### **PAPER**

### Multicolor dye-based flow structure visualization for seal-whisker geometry characterized by computer vision

To cite this article: Ondřej Ferčák et al 2024 Bioinspir. Biomim. 19 016004

View the article online for updates and enhancements.

### You may also like

- Estimation of Relative Transport Properties in Porous Transport Layers Using Pore-Scale and Pore-Network Simulations Seongyeop Jung, Mayank Sabharwal,
- Rayleigh—Taylor mixing: direct numerical simulation and implicit large eddy

simulation David L Youngs

Alex Jarauta et al.

 Statistics of the Navier—Stokes-alpha-beta regularization model for fluid turbulence Denis F Hinz, Tae-Yeon Kim and Eliot Fried

### Bioinspiration & Biomimetics



RECEIVED 28 July 2023

REVISED

16 October 2023

ACCEPTED FOR PUBLICATION 8 November 2023

PUBLISHED

17 November 2023

#### **PAPER**

# Multicolor dye-based flow structure visualization for seal-whisker geometry characterized by computer vision

Ondřej Ferčák<sup>1,\*</sup>, Kathleen M Lyons<sup>2</sup>, Christin T Murphy<sup>3</sup>, Kristina M Kamensky<sup>3</sup>, Raúl Bayoán Cal<sup>1</sup> and Jennifer A Franck<sup>2</sup>

- Department of Mechanical & Materials Engineering, Portland State University, Portland, OR, United States of America
- Department of Engineering Physics, University of Wisconsin-Madison, Madison, WI, United States of America
- <sup>3</sup> Naval Undersea Warfare Center Division Newport, Newport, RI, United States of America
- \* Author to whom any correspondence should be addressed.

E-mail: ofercak@pdx.edu

Keywords: pinniped vibrissae, dye-visualization, vortex tracking, computer vision

Supplementary material for this article is available online

### **Abstract**

Pinniped vibrissae possess a unique and complex three-dimensional topography, which has beneficial fluid flow characteristics such as substantial reductions in drag, lift, and vortex induced vibration. To understand and leverage these effects, the downstream vortex dynamics must be studied. Dye visualization is a traditional qualitative method of capturing these downstream effects, specifically in comparative biological investigations where complex equipment can be prohibitive. High-fidelity numerical simulations or experimental particle image velocimetry are commonplace for quantitative high-resolution flow measurements, but are computationally expensive, require costly equipment, and can have limited measurement windows. This study establishes a method for extracting quantitative data from standard dye visualization experiments on seal whisker geometries by leveraging novel but intuitive computer vision techniques, which maintain simplicity and an advantageous large experimental viewing window while automating the extraction of vortex frequency, position, and advection. Results are compared to direct numerical simulation (DNS) data for comparable geometries. Power spectra and Strouhal numbers show consistent behavior between methods for a Reynolds number of 500, with minima at the canonical geometry wavelength of 3.43 and a peak frequency of 0.2 for a Reynolds number of 250. The vortex tracking reveals a clear increase in velocity from roll-up to 3.5 whisker diameters downstream, with a strong overlap with the DNS data but shows steady results beyond the limited DNS window. This investigation provides insight into a valuable bio-inspired engineering model while advancing an analytical methodology that can readily be applied to a broad range of comparative biological studies.

### 1. Introduction

The vibrissae (whiskers) of harbor seals, and most other phocid seal species, are comprised of a pattern of complex three-dimensional undulations which are unique to this group. These undulated contours provide beneficial fluid flow characteristics including substantial drag reduction, oscillating lift force reduction, and shifting vortex-shedding to lower frequencies when compared to smooth profiles [1–4]. The geometric parameters that describe this topography, and the effect they have on flow properties, however,

have only recently started to be examined. These studies are mostly comprised of qualitative analog (experimental), or quantitative digital (numerical), methodologies with little to no overlap [3, 5–7]. The present study introduces a hybrid method, which is demonstrated by combining a qualitative dye-visualization experiment with open-source computer vision (CV) techniques, to digitally characterize and quantify flow response over the bio-inspired undulated profiles.

Fluid flow visualizations have relied on human vision for qualitative analysis of water, dye, or smoke flow behavior since the 1400's [8]. This approach

has fallen out of favor with the rise of computational power and highly specialized experimental equipment. For example, particle image velocimetry (PIV) and computational fluid dynamics (CFDs), can provide extremely detailed quantitative information about the fluid flow far beyond human visual ability. However, PIV requires extensive training, timeconsuming setup, and high cost and the increased fidelity of CFD, such as large eddy simulations and direct numerical simulations (DNSs), still have high computational cost and, therefore, require high performance computing systems. On the other hand, dye is still used reliably for fluid visualizations, specifically in comparative biological investigations, like the work of Gilpin et al [9] who used long exposure dye visualization with a novel open-source software to look at microfluidic structures of starfish larvae [10-14]. Dye has also been used in combination with PIV, simulations, or machine learning such as Raissi et al [15] who trained a deep-learning framework to recognize velocity and pressure fields from dye and smoke experimental studies [16–18].

The methodology used to characterize the flow response over the pinniped geometry in this study fills a gap between classic dye experimentation and computationally expensive simulations, PIV, or a combination thereof by leveraging readily available, lean, open-source CV software. This approach is used in parallel with DNS data for analysis and methodological comparison where applicable.

Research into vibrissae-inspired profiles is relatively new, but investigations into sinusoidal, wavy, or undulated bluff-bodies utilizing visually inspected photographs, time-exposure photography, and dye visualization have provided insight of potential benefits [19-21]. Some care must be taken when analyzing dye visualized flows since the dye motion can differ from the underlying flow [22, 23]. Nevertheless, dye is invaluable when cost, safety, time, and equipment are prohibitive. Further, the use of multiple dye-colors is a distinct advantage that comparable CFD results have difficulty implementing. The use of multi-color dye has been exploited by researchers to visualize a wide variety of flows [24-27]. Beyond biological studies, aeronautical research often employs the use of multiple dye colors to visualize distinct streak-lines and vortical structures [28–30].

The current work characterizes the effect of seal whisker geometry on coherent vortex structures and proposes several quantitative analysis methods using CV techniques from multi-color dye-based flow videos. First, the whisker-inspired geometries are defined, and details of the computational and experimental setups are presented in the experimental methods section. Then, the quantitative methods are outlined in the data analysis techniques subsections: color segmentation, Lagrangian vortex tracking, and background subtraction. Flow parameters

of seal whisker topography and wavelength modifications are investigated in the results section using the dye visualization, CV, and CFD methods. The conclusions section includes context and discussion.

### 2. Experimental methods

### 2.1. Model definition

The baseline undulated elliptical geometry is defined by seven geometric parameter values based on the work of Hanke *et al* [1]. The geometric parameters have been redefined and nondimensionalized such that they are independent from one another as detailed in the work by Lyons *et al* [5] and are summarized in figure 1.

Borrowing from aerodynamic terminology, the chord C is the width of the undulated cylinder model in the streamwise direction (x-coordinate) and the thickness T is the width of the model in the transverse direction (y-coordinate) (figure 1(d)). The geometry contains two spanwise undulations, one each in chord and thickness, with their own amplitude,  $A_C$  and  $A_T$  respectively. Both amplitude terms, as well as the periodicity of the geometry, which is governed by the wavelength  $\lambda$ , are normalized by thickness T.

Five whisker geometries are shown in figure 1; a baseline whisker geometry based on Hanke *et al* three additional models with wavelengths varying from the baseline, and an elliptical cylinder with no undulations. All other wavelength models share the same normalized values of AC = 0.23, AT = 0.09, and T = 1.00 with only the value of  $\lambda$  changing. The elliptical cylinder has an equivalent aspect ratio of the baseline whisker but no undulation.

To quantify and discuss the results, the response of the flow over the undulated cylinder models is nondimensionalized with respect to the freestream velocity,  $u_{\infty}$ , and the mean hydraulic diameter,  $D_h$ . The hydraulic diameter for the ellipse is 1.28 and  $D_h$  increases (1.27, 1.27, 1.28, and 1.32) along with the respective  $\lambda$  values (1.00, 2.00, 3.43, and 6.87) visualized in figure 1.

Given the variation in diameter,  $D_h$  is calculated using the mean cross-sectional area and perimeter, in the same manner as Witte *et al* [2], among others [31, 32]. Thus, the Reynolds number is defined as,

$$Re = \frac{U_{\infty}D_h}{\nu} \tag{1}$$

where  $\nu$  is the kinematic viscosity of the fluid. The nondimensional time scales of vortex shedding can be characterized by a reduced frequency,

$$f^* = \frac{fD_h}{U_{\infty}},\tag{2}$$

where the Strouhal number, St, is defined in this context to be the strongest peak of the force frequency spectra.

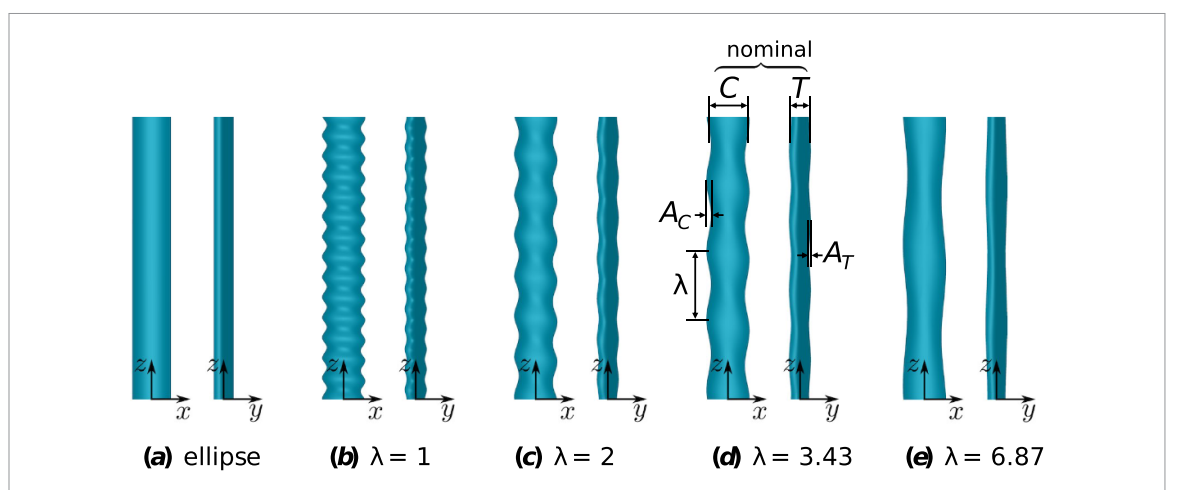


**Figure 1.** Top and side views of investigated models including smooth ellipse and undulated cylinder geometries with four unique wavelength,  $\lambda$  values, which govern the periodicity. The model corresponding to  $\lambda=3.43$  most closely matches the average measurements obtained from harbor seal whiskers and shows the remaining nondimensionalized parameters that define the seal whisker topography, where C is the average chord length and T is the average thickness. Undulation amplitudes along the chord length and thickness are given by  $A_C$  and  $A_T$ , respectively.

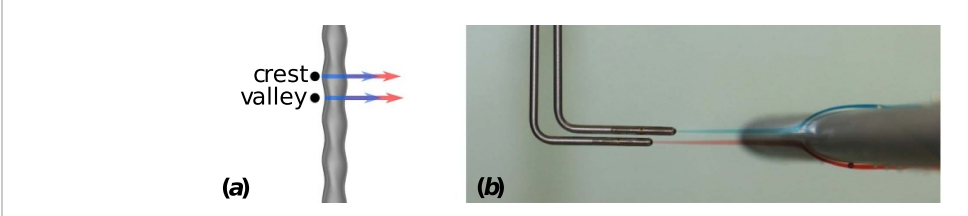


Figure 2. Dye probes release blue and red dye: (a) top view of two spanwise testing locations for each model, leading edge crest and leading edge valley. (b) Experimental view of two nozzles releasing blue and red dye.

### 2.2. Dye visualization setup

The water tunnel in the affiliated lab space is an open channel, 5689 l (1503 gal) recirculating system manufactured by Engineering Laboratory Design. The test section measures 225 cm  $(L) \times 45$  cm  $(W) \times 45$  cm (H) and is fitted with optical glass. Volumetric flowrates between 0.6075 and 465.75 l s<sup>-1</sup> and flow velocities between 0.003 and 2.3 m s<sup>-1</sup> are achievable.

Scale models with a mean chord length, C, of 1.32 cm, mean thickness, T, of 0.69 cm, and varying wavelength,  $\lambda$ , are created in clear acrylic resin using a stereolithography 3D printer. Each model is mounted horizontally in the tunnel within the first 50 cm of the test section from struts fixed to the rails at the top of the tunnel. After the model has been installed in the tunnel, coarse and fine adjustment in the vertical and lateral directions can be achieved at several locations in the fixtures for both the model and dye nozzles.

Red and blue dye are stored in two dye wells above the water tunnel. The dye is gravity fed and continuously released upstream of the model by two nozzles, blue above the center of the cylinder and red below the center of the cylinder, as shown in figure 2. The composition of the dye is as follows: for every 10 ml of water, one drop each of food coloring and isopropyl alcohol is used. The isopropyl alcohol helps to counteract the increase of density of the added food coloring in order to achieve the same density of water to provide accurate flow visualization. The hydrostatic pressure at the dye outlet is adjusted by modifying the mounting height of the wells above the water tunnel. The dye flow is further adjusted by a needle valve attached to each dye well. The location and angle of the dye ports can impact the dye trajectory, thus considerable effort is made to ensure the dye colors advect along the boundary layer. The dye port measures 0.159 cm in diameter and is carefully selected to achieve the necessary dye volumetric flowrate while minimizing flow disturbance.

For each geometry tested, the temperature of the water and the pump speed are measured and recorded. A Canon EOS 80D camera and Photron FASTCAM Mini high-speed camera are used to record video imaging of the dye in the flow over each model and in the near wake region. Each experimental video consists of 5K frames in total, a resolution of  $1024 \times 512$ , and a frame rate of 30 frames per second (fps). A typical vortex shedding cycle occurs over 100 frames (e.g.  $\lambda = 3.43$ , Re = 500). While the CV algorithm itself is not affected by the number of frames per cycle, it is preferable to have more than a minimum of 20–30 frames for a typical camera setup. Fewer frames may not be enough to smoothly

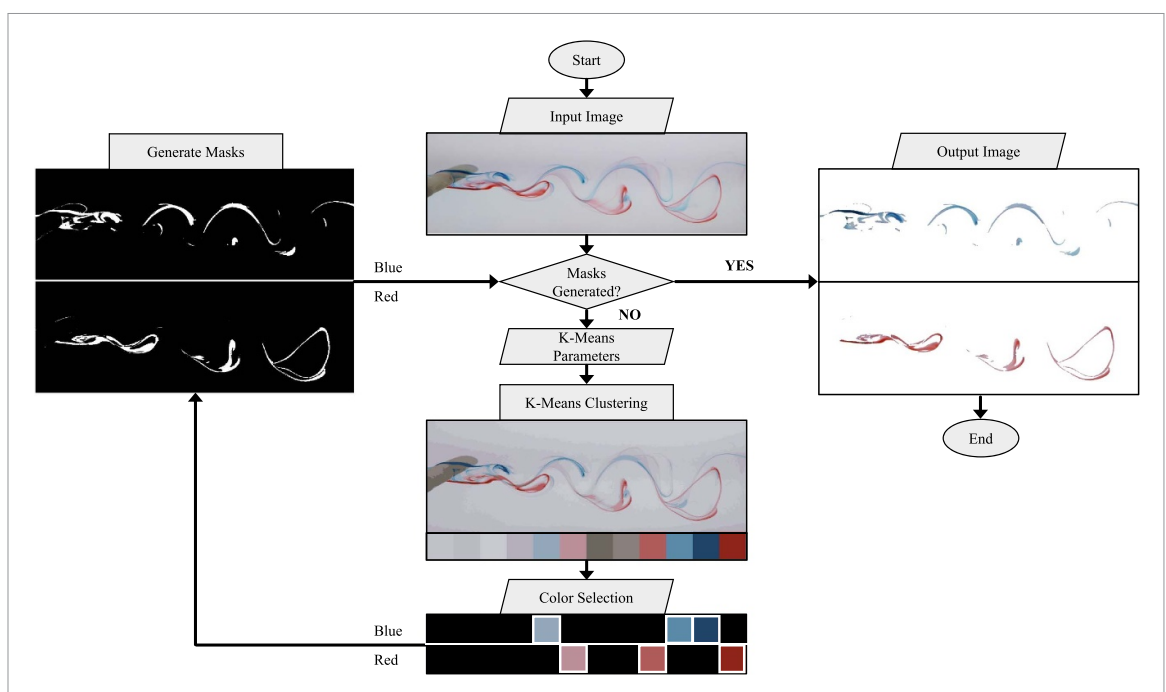


**Figure 3.** The color segmentation process includes an input image whose color range is binned into a specified number of RGB color ranges using K-means color quantization. The colors are then used to create any number of user defined masks, which are then used on the original image to extract the desired color. Shown here is  $\lambda = 6.87$ , Re = 250, at a peak position.

resolve velocity and acceleration components for vortex advection. A grid poster with known dimensions of  $2.5 \times 2.5$  cm is mounted to the outer backside of the test section to allow for image pixel scaling and help with fixture alignment. Velocity calibration is completed by the manufacturer from the factory using laser Doppler velocimetry. Local velocity is confirmed by highly repeatable timed dye tracking over the test section length of 1.5 m.

Dye visualization data are collected for the baseline model and the three modified configurations,  $\lambda = 1.00, 2.00, 3.43$ , and 6.87. Each of the models in the current study is observed at two flow speeds. The low speed is equivalent to Re = 215-250 and are referred to as Re = 250 throughout the text as flow variations within this Re range are negligible. Data is also recorded at a second, higher speed flow, approximately equivalent to Re = 500. Because the model geometry varies significantly along its span, two spanwise locations are recorded for each configuration. The first recording is taken when the dye is incident on a leading-edge crest and the second is taken when the dye is incident on a leading edge valley. All configurations are tested at zero angle-of-attack with the oncoming flow.

### 2.3. Data analysis techniques: color segmentation

The dye visualization videos are analyzed frame-byframe with standard CV methods using an opensource image processing library (OpenCV) in the Python programming language [33]. The methods discussed, however, can easily be implemented via similar libraries in a variety of programming languages.

In order to extract as much relevant data as possible from the images, the primary step in analysis requires either distinguishing the flow in question from the stationary background (background subtraction), or distinguishing the individual dye-colors from each other (color detection), or a combination of both. In this section, accessible and robust color segmentation methods are discussed, and background subtraction is discussed in the next section.

The concept of isolating red, blue, and green (RGB) pixel intensities (0–255) is relatively simple. However, this task can be fraught with frustration since real world, or experimental, images have a broad range of pixel intensities and overlap, making it difficult to isolate colors in a clean and efficient manner. Human vision is excellent at detecting colors in an image, partly because the distinctions can be compartmentalized, while a computer algorithm treats each pixel as a distinct color. To simulate human interpretation more closely, the colors that are represented in the image are reduced, or clustered, to a chosen total number of colors. This is achieved with a K-means color quantization summarized in figure 3.

First, the input image, or video frame, is loaded into the software in order to generate a mask for color segmentation. The example used in figure 3, is that of  $\lambda = 6.87$ , Re = 250, at a peak position. The K-means parameters, including the number of clusters  $\kappa$ , termination criteria  $\epsilon$ , and optional initialization criteria, are then input to initialize the color

Figure 4. Vortex identification process: (a) the original image snapshot. (b) Red dye segmentation. (c) Blue dye segmentation. (d) The original image snapshot with vortices highlighted. (e) Red segmentation after erosion and dilation. Green highlights the border of remaining structures, and red shows an enclosing circle satisfying the input criteria. (f) Blue segmentation showing process described in e. (g) The original image snapshot with vortices highlighted and inter-vortex distances displayed. (h) Red segmentation showing only the remaining structures and distances. (i) Blue segmentation showing process described in h.

quantization. The number of clusters is dependent on the image to be processed and requires some initial testing. Typical values range from  $\kappa = 8-15$ . The Kmeans algorithm is an iterative algorithm and the termination criteria  $\epsilon$  may be software dependent but is typically specified as the accuracy of the desired result (i.e. the convergence value of successive iterations). If the change between iterations is less than  $\epsilon$ , the algorithm will terminate. Other termination parameters can include a maximum iteration (in the case of no convergence) and initialization parameters. This study used  $\kappa = 12$  clusters, an accuracy termination criterion  $\epsilon$  of 0.05, a max iteration criterion of 30, and a center initialization technique based on Arthur et al [34]. Typical applications can use default termination criteria if included with the respective software library since their changes will be minimal compared to changes in  $\kappa = 8-15$ . Default criteria, for example, can range between  $\epsilon$  of 0.1–1.0, a maximum iteration criterion of 10-50, and a random center initialization technique.

Once the RGB values are calculated for each of the clusters (e.g.  $\kappa = 12$ ), they can be used for color segmentation as the user chooses. For this study, three separate hues were chosen for both blue and red dye colors as seen in figure 3. These hue choices are then used to generate masks for the blue and red dyes from the clustered image. The masks are then used on the original image to extract the full range of colors that make up the hues in question. Since the distances in the image are inherently in pixels, a reference, or calibration, image needs to be taken with an object of known size to establish proper scaling, which is calculated at 0.185 cm/pixel for this study. These extracted colors can now be used for further analysis with respect to shape, size, distance, or motion of the specified dye.

# 2.4. Data analysis techniques: Lagrangian vortex tracking

When coherent structures such as vortices are visible in the isolated dye-color images, it is possible to

track these structures in a time series of images, making it possible to retrieve a simple Lagrangian tracking algorithm. For this to be effective, it is important to establish a flow that is not overly diffuse and shows structure coherence in the region of interest. In other words, if the dyed vortices are not distinct enough from the background, obscured, or missing such as in figure 3, they cannot be calculated from flow field vector data such as PIV, even if present. The vortices themselves need to be distinct for CV to identify them to obtain the benefits outlined in the methodology of this study. For similar reasons, this study uses the canonical  $\lambda = 3.43$  cylinder at Re = 500 for vortex tracking.

For each dye color, the images are first converted to a binary (0 or 255) image for ease of calculations, and a combination of morphological image transformations are used, specifically erosion and dilation, for vortex identification. A  $3 \times 3$  pixel kernel is used as a structuring element to implement 2D convolution for the following operations. Erosion removes noise in the image and any bordering pixels unbounded by like pixels, effectively shrinking the structures in the image leaving only the dominant ones. Dilation, the inverse to erosion, is then used to make the dominant structures more robust for further analysis. The surviving structures are fitted with a minimum enclosing circle, which is the smallest circle into which the structure shape can fit and is usually tangent to the structure at several points. This circle can now be used to quantify the roundness, size, and position of each structure as seen in figure 4.

To minimize outliers during vortex identification, a few reasonable assumptions are used to further filter the structures. These assumptions are parameterized to include each structure's maximum size, minimum size, and roundness. Since there is no machine learning involved in the algorithm, these limits are required in lieu of a more intensive training data set. The maximum and minimum sizes are estimated from initial test images where vortical scales can be visualized, where the minimum size should be large enough as to

avoid pixel scale noise (e.g. small dots versus vortices) and the maximum size should be small enough to avoid identification of simultaneous vortices or large-scale dye advection (e.g. large sections of the image). The roundness can easily be estimated by a ratio of areas between the minimum enclosing circle and the structure itself. The closer the ratio is to one, the more round the structure and, therefore, more likely to contain a vortex. These parameters need to be fine-tuned by the user but are intuitive and easy to implement due to the immediate visual feedback. Once the algorithm is established, the minimum enclosing circle centers can be used to quantify vortex position and identification.

## 2.5. Data analysis techniques: background subtraction

A complimentary method for extracting dye motion from image frames is background subtraction and is illustrated on a subset of dye data in this study. The input frames  $(V_{\rm in})$  are initially brightened  $(V_{\rm out})$  using inverse gamma correction of the form  $V_{\rm out} = V_{\rm in}^{1/2}$  seen in figure 5(a). To differentiate the dye from the background, each frame is compared with previous frames to establish changing and stationary portions of the image.

The algorithm implemented in this study utilizes an improved adaptive mixture of Gaussians based model as described by Zivkovic *et al* [35, 36]. The resulting frames show only the dye motion and are converted, where the resulting mask pixel values are black (0) for stationary pixels and white (255) for pixel motion similar to the previous masks (figure 5). The mask pixels known to be outside of the dye wake are forced to black to avoid outlier noise. Any singular pixel outliers are removed through a median blur, which is a 2D convolution with a  $7 \times 7$  kernel used to replace a pixel value with a median value.

The masks are then used to calculate frequency spectra by using the vertical motion along the upper and lower edges of the dye. Vertical pixel motion is collected at eight fixed horizontal locations spaced relative to the whisker center, which is indicated by the white line in figure 5. Four locations are used to capture the upper edge of the wake (red) and four for the lower edge (blue). The eight locations are spaced asymmetrically to prevent wavelength synchronization. The upper probes are placed at  $x/D_h$  values of 4.41, 5.20, 6.37, and 8.33 while the lower probes are positioned at 4.45, 5.28, 6.62, and 8.82.

Any outliers or missing positional data are replaced with their preceding values. The power spectral density (PSD) is then calculated using Welch's method using a Hann window size of two-thirds of the data length, a two-thirds overlap, and 10K zero-padding [37]. The eight data sets are then averaged together and peak frequencies above thresholds of 0.1

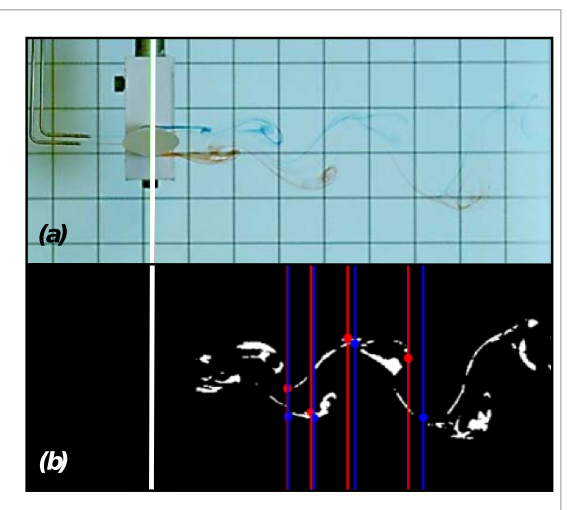


**Figure 5.** Frequency analysis process: (a) image initialization with brightness optimization, assignment of a streamwise cylinder-centered datum (white line), and mask creation. (b) Mask with red and blue line probes to capture upper and lower dye motion.

and 0.35 for Re = 250 and Re = 500 are documented, respectively.

#### 2.6. Direct numerical simulations

The CV analysis is compared to the DNSs performed by Lyons *et al* [38]. The computations simulate the flow field around the six geometric models investigated, by solving the incompressible Navier–Stokes equations using the open-source software OpenFOAM [39]. Full details on the numerical schemes, mesh resolution, and validation are provided in references Lyons *et al* [38] and Yuasa *et al* [40] but are summarized here in brevity.

A three-dimensional two-wavelength spanwise periodic computational domain is utilized, simulating an infinite span whisker profile, and neglecting any tip effects. The mesh generation process of Yuasa *et al* [40] maintains a structured body-fitted mesh for the precise undulation geometry. The total mesh size is 4.14M cells for the baseline model, and decreases/increases with respect to wavelength due to the variation in total span across the various models. The results have been previously validated against prior whisker simulation data using the mean drag and RMS lift forces.

### 3. Results

### 3.1. Qualitative observations of dye visualization

Before discussing CV analysis, the flow is qualitatively observed with respect to the two independent variables, Reynolds number Re and wavelength  $\lambda$ , to establish overall trends. Regardless of the geometric whisker model, several differences are apparent when comparing dye traces at different Reynolds numbers. At the lower Re = 250, the dye forms shear layers that oscillate in the *y*-direction as they move downstream. These layers remain largely connected forming wavy

**Figure 6.** Time progression of flow over the  $\lambda=3.43$  model behind the crest location: (a) dye traces form oscillating shear layers at Re = 250. (b) At Re = 500, dye traces detach and roll up into more coherent vortices before diffusing and dissipating into chaotic structures downstream, marked with boxes and arrow respectively. Frames are chosen to capture a single shedding cycle, therefore time between frames approximately twice as long for Re = 250 as for Re = 500.

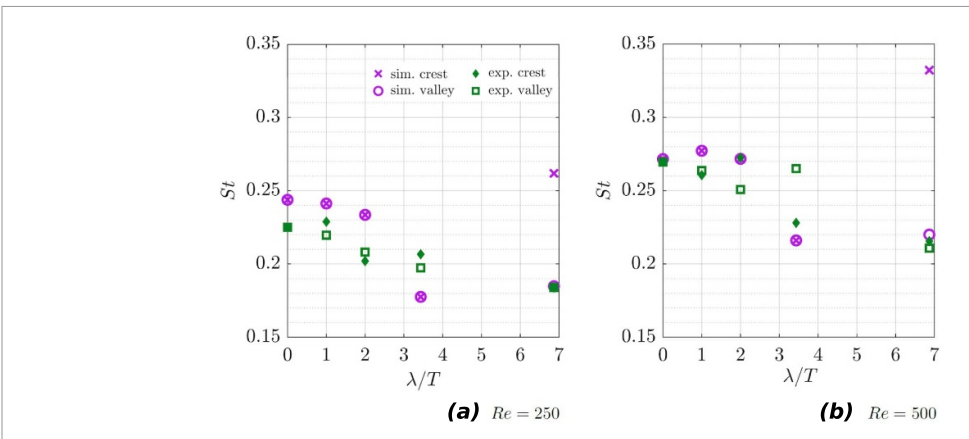


**Figure 7.** Comparison between calculated shedding frequencies from simulation and those computed from dye visualization video analysis shows a consistent downward trend of St with respect to  $\lambda$  up to  $\lambda = 3.43$ , the nominal seal whisker wavelength. The spanwise differences for the  $\lambda = 6.87$  model are captured within simulation results but are unresolved by the dye visualization analysis.

filaments in the wake as shown in figures 6(a) and 3. These wavy filaments are likely evidence of hairpin vortices, which are more prominently identified from the y–z plane, and are identified in the computational work of Liu *et al* among others [1, 6, 38].

At the higher Re = 500, the dye traces in the shear layers roll up and detach into more coherent vortices seen boxed in last panel of figure 6(b). A trend of detached structures is consistent across geometric models even though many of the flow patterns diverge from a typical von Kármán vortex street. In the downstream region of the high Re cases, more chaotic structures are visible such as those near the arrow also shown in figure 6(b), indicating increased turbulent fluctuations. Similar development of turbulent structures has been noted in dye visualization of flow over smooth circular cylinders, which transition to a turbulent wake [19].

### 3.2. Automated extraction of shedding frequency

Previous dye experiments could only provide a single shedding frequency calculated by manual vortex

counting, but with the use of CV analysis, a more resolved shedding spectrum is extracted from the unsteady phenomena. Although dye visualization can provide diagnostic cues for assessing the forces on the body, such as formation length and development of turbulent structures, drag and lift force calculations can only be determined through the inclusion of additional experimental sensors or numerical simulation and are thus not included here. A full discussion of lift and drag is detailed in Lyons *et al* [38].

Using the background subtraction methods described in the data analysis techniques subsection, background subtraction, unsteady flow patterns are quantified through analysis of the dye streaks. Images at both the geometric crest and valley whisker cross-sections are analyzed for all  $\lambda$  profiles at both Reynolds numbers. The PSD is computed for each image sequence, then the dominant, or peak frequency is non-dimensionalized as the Strouhal number (St) number and plotted in figure 7. Whisker crest and valley data points match well with one another, especially at low Re. At higher Reynolds number, this

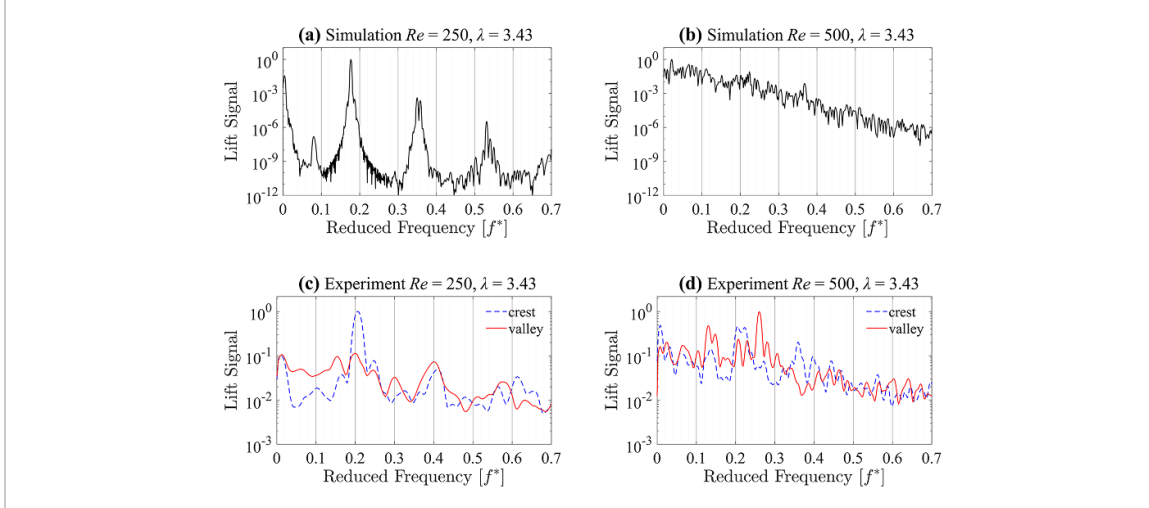


**Figure 8.** Power spectral density (PSD) for  $\lambda = 3.43$  share similar peak shape and location at Re = 250 for both simulation (a) and experiment (c). At Re = 500, PSD spectra follow a downward slope for both simulation (b) and experiment (d) but lack the distinctive nature of the peaks seen at Re = 250, resulting in an imprecise selection of St values for the  $\lambda = 3.43$  case at Re = 500 and the data spread seen in figure 7(b).

deviation between crest and valley is larger at the intermediate wavelengths,  $\lambda = 2$  and 3.43 but converge again at the highest wavelength.

The global trend for the dye frequencies is a drop in St with respect to  $\lambda$ , consistent across both Reynolds numbers. For comparison the DNS frequency spectra is extracted from a transverse velocity probe directly downstream of the body using the simulation data from Lyons *et al* [38], at the same geometric crest and valley locations.

The simulations reveal a similar trend, with the Strouhal number decreasing with respect to wavelength. However, the decrease is more extreme for the DNS data, ranging from St = 0.242 to St = 0.177, whereas the dye data is St = 0.228 to 0.183 for low Re, while at high Re measurements, the dye follows DNS more closely. Furthermore, the simulations display a rapid decrease between  $\lambda$  = 2 and 3.43 at both Reynolds numbers, whereas the decrease in experimental measurements is more gradual between  $\lambda$  = 1 and 3.43.

The simulation data also reveals that the valley and crest locations produce the same dominant frequency for all cases except  $\lambda = 6.87$ . Both figures 7(a) and (b) show the alignment of the purple markers for  $\lambda <= 3.43$  and then a sudden diversion at the largest ( $\lambda = 6.87$ ) wavelength. Further inspection of the simulation data at  $\lambda = 6.87$  reveals competing frequencies around  $f^* = 0.18$  and 0.26 (figure 9), and both are present at the crest and valley probes, with one slightly stronger than another. The dye visualization calculations are not able to discern the two frequencies along the span, and only pick up the lower of the two frequencies. The simulations are able to maintain perfect symmetry, while the dye data are affected by various real-world factors such as model precision, deviations in angle of attack, intermittent flow instabilities, and background noise in the water tunnel.

The spread between dve calculated frequencies for the  $\lambda = 3.43$  at Re = 500 and  $\lambda = 6.87$  for both Reynolds numbers are larger than observed for the other cases. Therefore, the  $\lambda = 3.43$  and  $\lambda = 6.87$  case are analyzed in more detail to gain a better understanding of the flow. To fully compare the frequency content contained in collected dye visualization data for  $\lambda = 3.43$ , a PSD is calculated for the simulated lift signal in the same manner as the dye visualization pixel locations outlined in the background subtraction subsection. The PSD plots for Re = 250 in figures 8(a) and (c) show distinct peaks near  $f^* = 0.2$ for both the simulation and experimental data. A secondary peak in the simulation results near  $f^* = 0.35$ also appears in the dye data albeit with a less distinct and broader peak.

For Re = 500, the same geometry displays a more complex lift spectra with broad peaks and gentle slopes rather than steep sharp peaks as seen in figure 8(b), and a dominant peak from the simulation data is difficult to discern. The PSD trends for the dye analysis are shown in 8(d) and follow a similar downward slope at higher frequencies and both plots are noticeably noisier than the Re = 250 case.

Similarly, a PSD is calculated for  $\lambda = 6.87$  and shown in figure 9. At Re = 250, both the simulation (a) and experimental (c) spectra show large prominent peaks at just under  $f^* = 0.2$ , including the experimental crest location, albeit with a reduced magnitude. However, the DNS data shows a repeating pattern of large peaks, decreasing in magnitude to either side of the dominant frequency. This behaviour is likely to produce competing frequencies such as the one around  $f^* = 0.27$  seen in figure 9(a). The spectra showing Re = 500 in figures 9(b) and (d) are comparable to the Re = 500 data in figure 8, where a more noisy downward slope is observed. The main distinction between  $\lambda = 3.43$  and  $\lambda = 6.87$  is that the latter

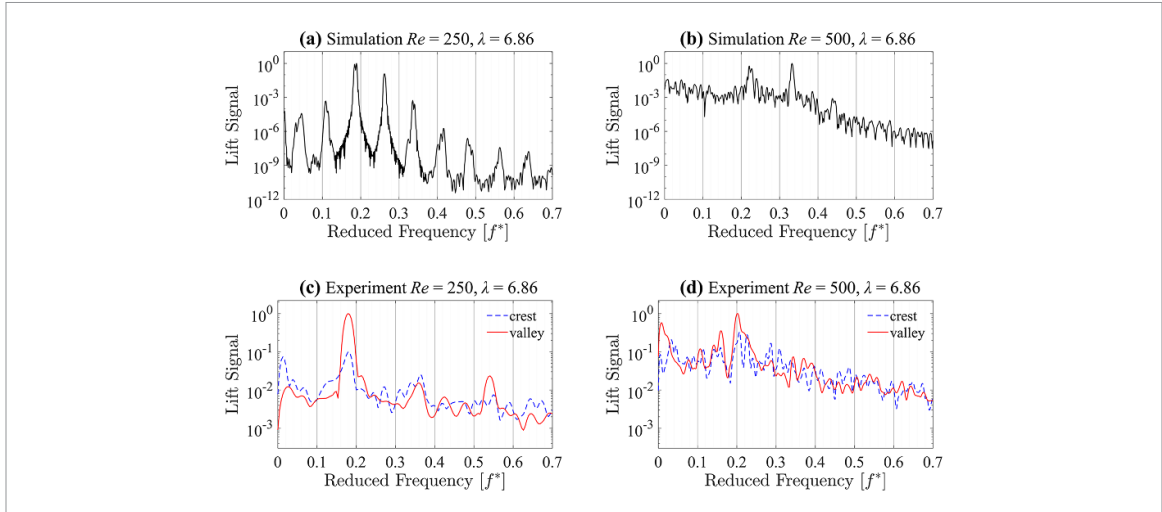


**Figure 9.** Power spectral density (PSD) for  $\lambda = 6.87$  share similar peak shape and location at Re = 250 for both simulation (a) and experiment (c), but the simulation reveals additional decreasing peaks on either side at constant frequency intervals. At Re = 500, PSD spectra follow a downward slope for both simulation (b) and experiment (d) but while the peaks for the experiment are approximately at the Re = 250 range, the magnitudes are small and the simulation is inconsistent.

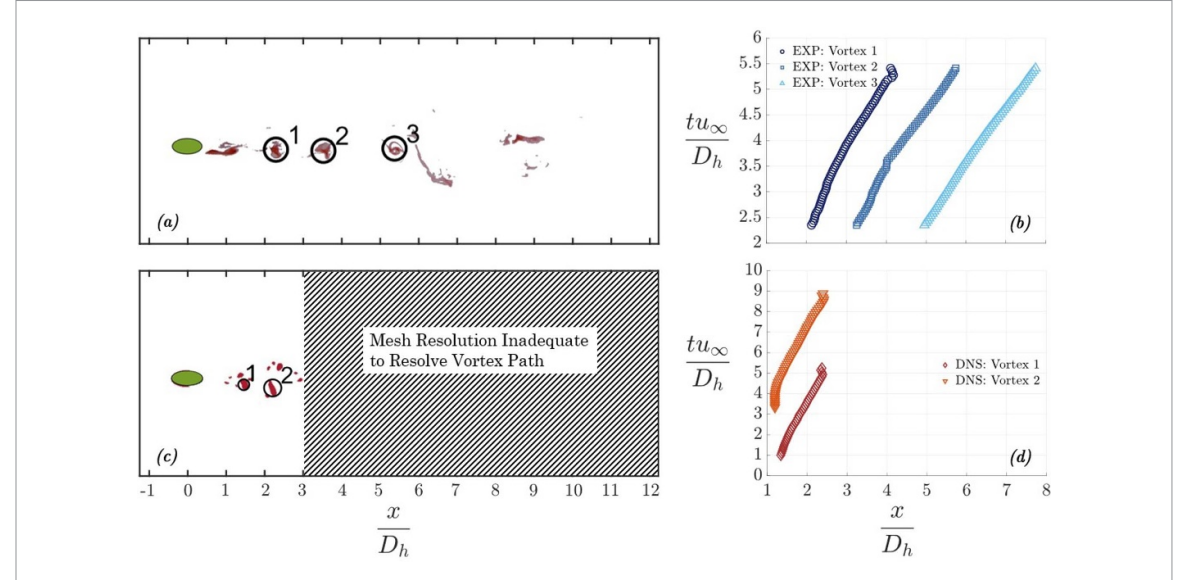


**Figure 10.** Tracked vortices at position  $\delta_\omega/D_h$ , and convective time,  $tu_\infty/D_h$ , for  $\lambda=3.43$  and Re = 500. (a) Normalized dye position snapshot. (b) Normalized dye position data. (c) Normalized DNS position snapshot (vertical lines in snapshot indicate region of poor mesh resolution in DNS analysis). (d) Normalized DNS position.

shows more prominent and competing peaks with a higher frequency near  $f^* = 0.32$  slightly larger than the other peak near  $f^* = 0.22$ .

### 3.3. Lagrangian vortex advection

To avoid reliance on user vision and automate vortex identification while limiting computational cost, the Lagrangian vortex identification and tracking algorithm described in the data analysis techniques subsection, Lagrangian vortex tracking is used to track three vortices as they move through time. Figure 10(b) shows a snapshot of the tracking results and positional data for the red dye. The choice of dye color is arbitrary, and symmetry is assumed for advection of the vortices visualized by the blue dye in the streamwise direction. Vortices show slight

displacement in the vertical direction, but this magnitude is negligible compared to the streamwise displacement and will, therefore, be excluded from the following analysis. Vortex 1 (figure 10) is seen forming behind the whisker and vortices 2 and 3 can be seen advecting at different rates downstream.

The position of each vortex in the streamwise, x-direction, through time is also seen figure 10. The x-position is non-dimensionalized by the cylinder hydraulic diameter,  $D_h$ , and time, t, by the free-stream velocity,  $u_{\infty}$ , and  $D_h$ . Vortex 1 moves a distance of  $D_h \approx 0.7$  downstream by  $tu_{\infty}/D_h \approx 3.6$ , which is similar to the distance covered by vortex 2. However, vortex 2 covers more distance for the remaining time of  $D_h \approx 1.7$  versus that of  $D_h \approx 1.1$  for vortex 1. Vortex 3 on the other hand can be seen to move in

a linear, or constant, increase in position per time for the entire duration. Compared to vortex 1 and 2, for the first time interval discussed ( $tu_{\infty}/D_h \approx 3.6$ ), vortex 3 shows the largest increase in distance of  $D_h \approx 1.1$  and continues to cover a distance for the remaining time of  $D_h \approx 1.7$ , which is comparable to the tail end of the increase in position for vortex 2.

For comparison, DNS data showing Q-criterion structures is tracked with the same algorithm, a snapshot of which can be seen in figure 10(c). Q-criterion is defined here as the second invariant of the velocity gradient tensor,  $\partial u_i/\partial x_j$ , calculated from the vorticity and rate-of-strain tensors as defined by Haller [41]. While Q-criterion and dye are not visualizing the same phenomena, Q-criterion is good at showing vortex cores and is, therefore, a suitable quantity to track for comparison with the dye vortices. Due to the computational expense of DNS, the data from the simulations is limited to the region directly behind the whisker cross-section up to 3D downstream, where mesh stretching begins to numerically dissipate vortex structures (figure 10(d)). It should also be noted that although the DNS is three-dimensional, a two-dimensional slice is analyzed and thus can only reveal motion in the streamwise direction. In contrast, the dye has engulfed multiple z-planes due to the width and diffusion of the dye, many of which are captured simultaneously by the camera image. These differences should be noted when discrepancies between methods are considered.

The two tracked vortices move in mostly linear increments through time (figure 10), although the retrieved DNS positions are much closer to the undulated geometry than the dye experiment. In fact, this is a limitation of DNS since a large computational domain is expensive, while dye experiments are limited by camera position and flow coherence.

To investigate the motion of the vortices further, the distance,  $\delta_{\omega}$ , between vortex 1 and vortex 2 (Vortex 1-2), and between vortex 2 and 3 (Vortex 2–3) is shown in figure 11(a). The normalized downstream distance  $x/D_h$  is referenced from the upstream vortex position from each vortex pair and  $\delta_{\omega}$  is normalized by the hydraulic diameter  $D_h$ as before. The distance between vortex 1-2 displays a sharp increase from formation to a position of  $D_h \approx$ 3.5 with a power of 0.21 seen in the first black linear fit in figure 11(a). Vortex 2-3 shows the same trend for values upstream of  $D_h \approx 3.6$  indicating a cyclic vortical behavior. The distance between vortex 2-3, however, becomes effectively constant from  $D_h \approx 3.6-5.2$ , as seen with the downstream black linear fit in the figure, suggesting that the intervortex distance is steady for downstream distances beyond  $D_h \approx 3.6$ .

In contrast to the dye, the DNS data is limited to the near wake, and exhibits a much sharper increase from  $D_h \approx 1.8-2.2$  than the dye results. One reason

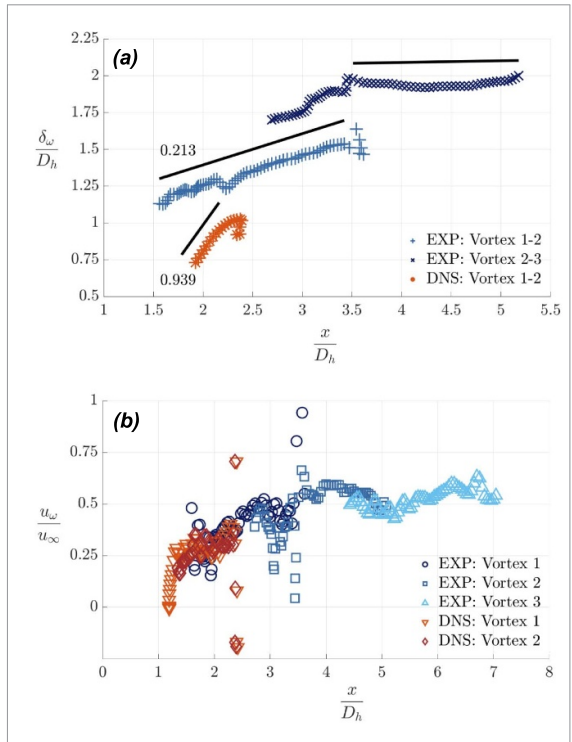


**Figure 11.** (a) Normalized vortex distances  $(\delta_{\omega}/D_h)$  as a function of position  $(x/D_h)$  for  $\lambda=3.43$  profile and Re = 500. (b) Normalized vortex velocities  $(u\omega/u\infty)$  as a function of position  $(x/D_h)$  for  $\lambda=3.43$  profile and Re = 500.

for this disparity is likely due to the different metrics employed between the Eularian Q-criterion and the Lagrangian dye tracer tracking. Another reason may be due to the CFD representation of a two-dimensional *z*-plane slice of the domain. This means that the same Lagrangian particles are not necessarily captured because the dye is simultaneously diffusing through the *z*-planes.

From the position data, convection velocity of the vortices can be easily computed. The vortex velocities  $u_{\omega}$ , normalized by the freestream velocity,  $u\infty$ , are expressed as a function of the normalized downstream position  $x/D_h$  in figure 11(b). It can be seen that there is a large initial disparity between vortex 1 and 2 velocities, with vortex 1 starting at  $u_{\omega}/u_{\infty} \approx$ 0.24 while vortex 2 starts out much faster at  $u_{\omega}/u_{\infty} \approx$ 0.4. However, vortex 1 increases in velocity significantly up to  $u_{\omega}/u_{\infty} \approx 0.5$  for  $D_h \approx 3$ , while vortex 2 only increases to  $u_{\omega}/u_{\infty} \approx 0.6$  by  $D_h \approx 4.2$  and then levels off. This is consistent with the trend seen in figure 11(a), where the vortex distances become steady. More outliers are visible around this transition point of  $D_h \approx 3.4$ , while the velocity becomes more consistent farther downstream. Vortex 3 is seen to hold a more constant velocity throughout with minor deviations indicating a steadier state behavior.

DNS vortex 1 starts close to zero initial velocity at  $D_h \approx 1.2$  and accelerates to  $u_\omega/u_\infty \approx 0.24$  to match the other vorticities at the same position downstream.

There is clear overlap with DNS vortex 2 and the experimental vortex 1 between  $x/D_h$  of 1.4–2.4. Since the the vortex velocities display good agreement, it is reasonable to attribute the slow initial velocity of DNS vortex 1 to the vortex rollup and formation above and below the geometry cross section and that the increase in velocity occurs once the vortex sheds, or detaches, from the shear layers seen in the images.

### 4. Conclusions

Open-source and accessible CV methods are used for analysis of flow over pinniped vibrissae-inspired geometry. This study is not meant to be an exhaustive study of CV algorithms, rather, available techniques are highlighted to show the potential speed and reliability of these methods for extraction of fundamental flow information from experimental images frames. Additional algorithms can easily be adapted to the specific needs of experimentalists beyond this study. This type of analysis allows researchers to reduce their reliance on human vision and expensive computations, which fills a middle ground often missing for experimental studies. Further specialization can include a broader range of dye tracking, wake growth quantification, or the addition of lean machine-learning algorithms.

The flow behavior observed in the qualitative observations of dye visualization reveals a clear Reynolds number dependence, specifically vortex roll-up and formation at Re=500 versus oscillating shear layer flow at Re=250 for the geometry most closely resembling that of the pinniped vibrissae ( $\lambda=3.43$ ). The formation of coherent vortices behind the cylinder followed by downstream diffusion and mixing of the dye are also seen. Both DNS and dye visualization qualitatively reveal that the whisker topography increases spanwise flow when compared to a smooth ellipse, even at small wavelengths.

Further quantitative analysis is difficult, however, without the aid of computational methods. Two distinct computational methods were employed in this study, CV on the aforementioned dye images and DNSs on comparable cylindrical geometries.

Shedding frequencies for both CV and DNS methods show a consistent downward trend of the Strouhal Number (St) as a function of  $\lambda$ . The CV method outlined in background subtraction subsection is in high agreement with the DNS data and more computationally efficient for calculating the Strouhal Number for all cases below  $\lambda = 6.87$ . Since the wakes of the lower lambda values have continuous boundary layers present at the edges of the wake, the background subtraction method can easily find the frequencies at the wake edges, which is not the case for  $\lambda = 6.87$ , where that edge is not resolved due to diffusion of the dye. This suggests that the canonical

 $\lambda = 3.43$  geometry is optimal for reducing oscillatory frequency and therefore, vibration of the cylinder.

For this optimal  $\lambda = 3.43$  case, the full PSD is also extracted, and the CV method produced similar trends to that of the DNS data at a fraction of the time. The peak frequency response for the cylinders is at 0.2 for Re = 250, which is confirmed by both methods. DNS data for the Re = 500 case trend downward in a similar manner as the CV data and a dominant frequency is not discernible from the DNS data for comparison. There are peaks ranging from 0.2 to 0.4 suggesting a comparable frequency response with Re = 250 but larger amplitude variation is also present, so confirmation of peak response is unclear. What is clear is that the non-dimensional wavelength closest to biological measurements of seal whiskers  $(\lambda = 3.43)$  exhibited a higher degree of force reduction properties when compared other  $\lambda$  values.

Vorticity, Q-criterion, and critical-point calculations can be done via simulations but are computationally expensive. Tracking experimental dye vortices using simple CV techniques can be more time consuming than background subtraction depending on the K-means color quantization parameters used. However, there are several benefits of CV for this analysis.

Counting vortices by hand in each frame is time prohibitive and prone to human error. Tracking separate dye colors individually is not possible with DNS and the computational domain for simulations can also be limited, which means that resolving flow far down stream is usually limited. For example, in this study, the DNS data extended  $x/D_h = 5$  downstream, while the dye experiment's field of view included up to  $x/D_h \approx 14$ .

The wide experimental field of view showed a fast increase of the vortices behind the cylinder up to the point of steady velocity. Isolating the vortices is susceptible to error if the vortices are not coherent enough or if the dye is too diffuse, but since the nature of vortices is such that they are coherent, this method is reliable and comparable to Q-criterion visualization. A full scale Re and  $\lambda$  comparison is, therefore, not reasonable for all the cases, since coherent vortices were not present in all cases.

For  $\lambda=3.43$ , the region directly behind the cylinder has a reduction of vortex velocity,  $u_{\omega}$ , relative to the inflow velocity  $u_{\infty}$  but recovers shortly by  $x/D_h\approx 6.75$  where  $u_{\omega}$  becomes steady. This behavior is further corroborated by the vortex spacing,  $\delta_{\omega}$ , which illustrates how the downstream vortices accelerate in the low pressure region behind the cylinder and catch up to each other downstream. This fast wake recovery visualized by the vortices along with their subsequent dissipation within a single frame, provides additional validation of the benefits of this undulated cylinder topography. This geometry has a wide range of application potential including industrial mixing, combustion, and chemical reactions,

underwater marine applications where oscillation or vibration reduction is needed, structures that require limited wake formation, and potential improvements to bio-inspired sensors and biomimetic underwater vision [42–46].

### Data availability statement

The data that support the findings of this study are openly available at the following URL/DOI: https://github.com/ofercak/Dye-Based-Flow-Structure-Identification.

### Acknowledgments

This work was funded in part by the National Science Foundation Awards 2035789/2037582 and the Naval Undersea Warfare Center (NUWC) In-house Laboratory Independent Research (ILIR) Program with support from the Office of Naval Research (ONR) Naval Research Enterprise Internship Program and the Summer Faculty Research Program. The authors are grateful for the technical guidance received from Dr William Martin, Dr Nathan Speirs, Dr Jesse Belden, Dr Aren Hellum, Dr Elizabeth Magliula, and Dr Tony Ruffa, and kindly thank William Haddock for design and fabrication of test section fixtures and dye mounts.

### **ORCID** iDs

Ondřej Ferčák https://orcid.org/0009-0008-0957-7929

Kathleen M Lyons 6 https://orcid.org/0000-0003-4099-2721

Jennifer A Franck https://orcid.org/0000-0001-8456-5153

### References

- Hanke W et al 2010 Harbor seal vibrissa morphology suppresses vortex-induced vibrations J. Exp. Biol. 213 2665–72
- [2] Witte M et al 2012 On the wake flow dynamics behind harbor seal vibrissae—a fluid mechanical explanation for an extraordinary capability Results of the DFG Priority Programme 1207 "Nature-Inspired Fluid Mechanics" 2006–2012 ed C Tropea and H Bleckmann (Springer) pp 271–89
- [3] Hans H, Miao J, Weymouth G and Triantafyllou M 2013 Whisker-like geometries and their force reduction properties 2013 MTS/IEEE OCEANS (Bergen, Norway) pp 1–7
- [4] Wang S and Liu Y 2016 Wake dynamics behind a seal-vibrissa-shaped cylinder: a comparative study by time-resolved particle velocimetry measurements Exp. Fluids 57 32
- [5] Lyons K, Murphy C T and Franck J A 2020 Flow over seal whiskers: importance of geometric features for force and frequency response PLoS One 15 e0241142
- [6] Liu G, Xue Q and Zheng X 2019 Phase-difference on seal whisker surface induces hairpin vortices in the wake to suppress force oscillation *Bioinspir*. *Biomim*. 14 066001
- [7] Assi G R S and Bearman P W 2018 Vortex-induced vibration of a wavy elliptic cylinder J. Fluids Struct. 80 1–21

- [8] Freymuth P 1993 Flow visualization in fluid mechanics Rev. Sci. Instrum. 64 1–18
- [9] Gilpin W, Prakash V N and Prakash M 2017 Flowtrace: simple visualization of coherent structures in biological fluid flows J. Exp. Biol. 220 3411–8
- [10] Dabiri J O, Colin S P, Costello J H and Gharib M 2005 Flow patterns generated by oblate medusan jellyfish: field measurements and laboratory analyses *J. Exp. Biol.* 208 1257–65
- [11] Green M H, Ho R K and Hale M E 2011 Movement and function of the pectoral fins of the larval zebrafish (Danio rerio) during slow swimming *J. Exp. Biol.* 214 3111–23
- [12] Weissburg M, Atkins L, Berkenkamp K and Mankin D 2012 Dine or dash? Turbulence inhibits blue crab navigation in attractive—aversive odor plumes by altering signal structure encoded by the olfactory pathway J. Exp. Biol. 215 4175–82
- [13] Carr Z R and Ringuette M J 2014 Flow structure of low-aspect-ratio rotating wings from dye visualization AIAA J. 52 1081–6
- [14] Haines G E and Sanderson S L 2017 Integration of swimming kinematics and ram suspension feeding in a model American paddlefish, Polyodon spathula J. Exp. Biol. 220 4535–47
- [15] Raissi M, Yazdani A and Karniadakis G E 2020 Hidden fluid mechanics: learning velocity and pressure fields from flow visualizations Science 367 1026–30
- [16] Lu Y, Shen G X and Lai G J 2006 Dual leading-edge vortices on flapping wings J. Exp. Biol. 209 5005–16
- [17] Dabiri J O, Colin S, Katija K and Costello J H 2010 A wake-based correlate of swimming performance and foraging behavior in seven co-occurring jellyfish species J. Exp. Biol. 213 1217–25
- [18] Sutherland K R and Madin L P 2010 Comparative jet wake structure and swimming performance of salps J. Exp. Biol. 213 2967–75
- [19] Gerrard J H and Lighthill M J 1978 The wakes of cylindrical bluff bodies at low Reynolds number *Phil. Trans. R. Soc.* A 288 351–82
- [20] Perry A E, Chong M S and Lim T T 1982 The vortex-shedding process behind two-dimensional bluff bodies J. Fluid Mech. 116 77–90
- [21] Ahmed A and Bays-Muchmore B 1992 Transverse flow over a wavy cylinder *Phys. Fluids* A 4 1959–67
- [22] Hama F R 1962 Streaklines in a perturbed shear flow *Phys. Fluids*  $5\,644-50$
- [23] Gursul I, Lusseyran D and Rockwell D 1990 On interpretation of flow visualization of unsteady shear flows Exp. Fluids 9 257–66
- [24] Merzkirch W 1974 Flow Visualization (Academic)
- [25] Karch G K, Sadlo F, Weiskopf D, Hansen C D, Li G-S and Ertl T 2012 Dye-based flow visualization Comput. Sci. Eng. 14 80–86
- [26] Kurada S, Rankin G and Sridhar K 1994 Flow visualization using photochromic dyes: a review Opt. Lasers Eng. 20 177–92
- [27] Jobard B, Erlebacher G and Hussaini M Y 2002 Lagrangian-Eulerian advection of noise and dye textures for unsteady flow visualization *IEEE Trans. Vis. Comput. Graph.* 8 211–22
- [28] Nelson R 1988 Visualization techniques for studying high angle of attack separated vortical flows 15th Aerodynamic Testing Conf. p 2025
- [29] Delfrate J H 1995 NASA Dryden flow visualization facility NASA Technical Memorandum 4631 (National Aeronautics and Space Administration) (Dryden Flight Research Center)
- [30] Thu A M, Byun Y H and Lee J-W 2012 Dye visualization of the vortical flow structure over a double-delta wing *J. Aerosp.* Eng. 25 541–6
- [31] Morrison H E, Brede M, Dehnhardt G and Leder A 2016 Simulating the flow and trail following capabilities of harbour seal vibrissae with the Lattice Boltzmann Method J. Comput. Sci. 17 394–402

- [32] Kim H and Yoon H S 2017 Effect of the orientation of the harbor seal vibrissa based biomimetic cylinder on hydrodynamic forces and vortex induced frequency AIP Adv. 7 105015
- [33] Bradski G and Kaehler A 2008 Learning OpenCV: Computer Vision with the OpenCV Library (O'Reilly Media, Inc.)
- [34] Arthur D, Vassilvitskii S and Gabow H 2007 Proceedings of the Eighteenth Annual ACM-Siam Symposium on Discrete Algorithms (Society for Industrial and Applied Mathematics)
- [35] Zivkovic Z 2004 Improved adaptive Gaussian mixture model for background subtraction Proc. 17th Int. Conf. on Pattern Recognition, 2004 (ICPR 2004) vol 2 (IEEE) pp 28–31
- [36] Zivkovic Z and Van Der Heijden F 2006 Efficient adaptive density estimation per image pixel for the task of background subtraction *Pattern Recognit. Lett.* 27 773–80
- [37] Welch P 1967 The use of fast Fourier transform for the estimation of power spectra: a method based on time averaging over short, modified periodograms *IEEE Trans.*Audio Electroacoust. 15 70–73
- [38] Lyons K, Cal R B and Franck J A 2023 Effects of wavelength on vortex structure and turbulence kinetic energy transfer of flow over undulated cylinders *Theor. Comput. Fluid Dyn.* 37 1–20

- [39] Weller H G, Tabor G, Jasak H and Fureby C 1998 A tensorial approach to computational continuum mechanics using object-oriented techniques Comput. Phys. 12 620–31
- [40] Yuasa M, Lyons K and Franck J A 2022 Simulations of flow over a bio-inspired undulated cylinder with dynamically morphing topography J. Fluids Struct. 111 103567
- [41] Haller G 2005 An objective definition of a vortex *J. Fluid Mech.*  $525\ 1-26$
- [42] y Alvarado P V, Subramaniam V and Triantafyllou M 2012 Design of a bio-inspired whisker sensor for underwater applications Sensors, 2012 IEEE (IEEE) pp 1–4
- [43] Beem H 2016 Seal whiskers inspire marine technology Ocean Mag. 51 82–85
- [44] Kottapalli A, Asadnia M, Hans H, Miao J and Triantafyllou M 2014 Harbor seal inspired MEMS artificial micro-whisker sensor 2014 IEEE 27th Int. Conf. on Micro Electro Mechanical Systems (MEMS) (IEEE) pp 741–4
- [45] Zheng X, Kamat A M, Cao M and Kottapalli A G P 2021 Creating underwater vision through wavy whiskers: a review of the flow-sensing mechanisms and biomimetic potential of seal whiskers J. R. Soc. Interface 18 20210629
- [46] Zhang X, Shan X, Xie T, Miao J, Du H and Song R 2021 Harbor seal whisker inspired self-powered piezoelectric sensor for detecting the underwater flow angle of attack and velocity *Measurement* 172 108866